Flexible and Cost-Effective Deep Learning for Fast Multi-Parametric Relaxometry using Phase-Cycled bSSFP

Florian Birk

florian.birk@tuebingen.mpg.de

Universitätsklinikum Tübingen

Lucas Mahler
Max Planck Institute for Biological Cybernetics

Julius Steiglechner
Universitätsklinikum Tübingen

Qi Wang
Max Planck Institute for Biological Cybernetics

Klaus Scheffler
Universitätsklinikum Tübingen

Rahel Heule
Universitätsklinikum Tübingen

Additional Declarations: No competing interests reported.

Flexible and Cost-Effective Deep Learning for Fast Multi-Parametric Relaxometry using Phase-Cycled bSSFP

Florian Birk[1,2,*], **Lucas Mahler**[2], **Julius Steiglechner**[1,2], **Qi Wang**[2], **Klaus Scheffler**[1,2], **and Rahel Heule**[1,2,3]

[1]Department of Biomedical Magnetic Resonance, University of Tübingen, Tübingen, Germany
[2]High-Field Magnetic Resonance, Max Planck Institute for Biological Cybernetics, Tübingen, Germany
[3]Center for MR Research, University Children's Hospital, Zurich, Switzerland
[*]florian.birk@tuebingen.mpg.de

ABSTRACT

To accelerate the clinical adoption of quantitative magnetic resonance imaging (qMRI), frameworks are needed that not only allow for rapid acquisition, but also flexibility, cost-efficiency, and high accuracy in parameter mapping. In this study, feed-forward deep neural network (DNN)- and iterative fitting-based frameworks are compared for multi-parametric (MP) relaxometry based on phase-cycled balanced steady-state free precession (pc-bSSFP) imaging. The performance of supervised DNNs (SVNN), self-supervised physics-informed DNNs (PINN), and an iterative fitting framework termed motion-insensitive rapid configuration relaxometry (MIRACLE) was evaluated in silico and in vivo in brain tissue of healthy subjects, including Monte Carlo sampling to simulate noise. DNNs were trained on three distinct in silico parameter distributions and at different signal-to-noise-ratios. The PINN framework, which incorporates physical knowledge into the training process, ensured more consistent inference and increased robustness to training data distribution compared to the SVNN. Whole-brain relaxometry using DNNs proved to be effective and adaptive, suggesting the potential for low-cost DNN retraining. This work emphasizes the advantages of in silico DNN MP-qMRI pipelines for rapid data generation and DNN training without extensive dictionary generation, long parameter inference times, or prolonged data acquisition, highlighting the flexible and rapid nature of lightweight machine learning applications for MP-qMRI.

Introduction

Improving the efficiency and stability of quantitative magnetic resonance imaging (qMRI) methods is a crucial research task to enable clinical applicability, necessitating sophisticated acquisition, reconstruction, and postprocessing strategies. In addition to accurate morphological information, which MRI as a non-invasive imaging tool can provide to guide treatment[1], qMRI has the potential to reduce subjectivity, resolve hardware or protocol dependencies inherent to conventional qualitative imaging, and increase intra- or interscanner reproducibility[2], facilitating the decision-making process in the diagnosis and prognosis of diseases. Generally, qMRI aims at fitting multiple qualitative (weighted) images to quantitative parameter maps with a voxel-wise representation of biophysical and microstructural processes. The derived quantitative MR biomarkers, such as relaxometry metrics, offer great potential for early detection of pathological tissue changes or longitudinal monitoring of disease. Recent studies have shown that quantitative T_2 is an important marker of cortical pathology in multiple sclerosis patients[3,4], early detection of hippocampal sclerosis in mesial temporal lobe epilepsy[5], cerebrovascular disease[6], or early Alzheimer's disease[7,8]. Quantitative T_1 has proven beneficial for longitudinal studies to access microstructural changes related to brain aging[9] or Parkinson's disease[10]. To reduce acquisition time, multi-parametric qMRI (MP-qMRI) has been of particular interest, aiming at the simultaneous estimation of multiple intrinsically co-registered parameter maps and a more complete neuroimaging protocol within feasible scan times[11,12].

Steady-state free precession (SSFP) sequences are a popular choice for MP-qMRI due to their sensitivity to various biochemical and microstructural tissue properties, mixed T_1 and T_2 signal sensitivity, and efficiency[13]. Jara et al. reported that MP-qMRI frameworks can be divided into direct and indirect frameworks. The latter rely on clinically interpretable fully reconstructed weighted images for post hoc mapping of parameters of interest[14–18]. On the other hand, direct MP-qMRI frameworks, such as magnetic resonance fingerprinting (MRF)[19], employ the acquisition of hundreds to thousands of data points using high undersampling factors to then quantify parameters of interest from the acquired tissue-specific signal evolutions. Thereby, MRF uses a pseudo-randomized pattern of continuously varying flip angles and repetition times, which is not necessarily efficient due to required relaxation delays to recover longitudinal magnetization. Recent studies

demonstrate whole-brain coverage using MRF, but at the cost of either prohibitively long combined image reconstruction and dictionary generation times in the order of a few hours[20] or rather low resolution with thick slices to ensure sufficiently high signal-to-noise-ratios (SNRs)[21,22]. Indirect approaches, including phase-cycled balanced SSFP (pc-bSSFP)[15,16] and multi-pathway non-balanced SSFP[14] imaging, allow fast and efficient acquisition of multiple contrasts without the need for extensive undersampling, waiting times, or long reconstruction times, while providing isotropic whole-brain coverage.

Machine learning (ML) techniques, in particular deep neural networks (DNNs), have shown great success for both direct and indirect MP-qMRI frameworks. DNNs are utilized for dictionary generation and matching in the case of MRF[22–24] or for multi-parametric inference from multi-contrast SSFP data[18,25]. Data-driven model-free methods that leverage measured input and ground truth data for supervised learning are capable of eliminating the estimation bias due to oversimplified existing signal models, for example as a result of unaccounted microstructural features as in the case of single-component simultaneous T_1 and T_2 quantification based on pc-bSSFP[18]. The primary constraints of in vivo supervised learning are the dependence of the trained DNN on specific measurement protocols, time-consuming acquisition of ground truth data, limited hardware and data accessibility, and unknown model assumptions as part of black-box modeling. In silico data generation, on the other hand, allows maximum control over the training data used and is becoming increasingly important in the (pre)training of ML models. Nevertheless, DNNs trained on in silico data for MP-qMRI are strongly influenced by the chosen training data distribution[26]. Gyori et al. showed that selecting a uniform or an in vivo data distribution for the target parameters of interest differently affects the precision and accuracy of supervised DNN predictions. Recent research has compared supervised deep neural networks with physics-informed self-supervised decoding-encoding deep neural networks in the context of joint diffusion and T_1 quantification[27].

This study proposes the use of in silico pc-bSSFP data to train DNN models as flexible and cost-effective frameworks for multi-parameter estimation. To this end, we compare three methods for in vivo whole-brain MP-qMRI relaxometry targeted on the simultaneous estimation of T_1 and T_2 in tissue, including a supervised DNN (SVNN), a physics-informed self-supervised DNN (PINN), and a conventional relaxometry method called motion-insensitive rapid configuration relaxometry (MIRACLE)[15] as reference. We investigate the impact of training data distribution on the reliability of the parameter estimation for both DNN methods. The robustness of the trained SVNNs and PINNs as well as conventional MIRACLE in the presence of noise-corrupted data is analyzed based on a Monte Carlo (MC) estimation of accuracy and precision metrics. Ultimately, we evaluate the flexibility of DNNs in learning the inverse signal model for parameter estimation in terms of convergence speed during training and estimation speed of the final DNN models.

Methods

The following subsections describe the in vivo data acquisition and processing, the in silico signal generation, the DNN and MIRACLE frameworks for relaxometry fitting, and the experiments to validate the in silico and in vivo performance. All in vivo experiments were conducted at a field strength of 3 T (Magnetom Prisma, Siemens Healthineers, Erlangen, Germany) and in accordance with the guidelines of the ethics committee of the Faculty of Medicine at the Eberhard Karls University of Tübingen. Python and PyTorch were used for data simulation, data processing, as well as DNN training and fitting.

Data Acquisition *In Vivo*

For in vivo validation, sagittal 3D pc-bSSFP data were used, acquired in healthy subjects with a $N_{pc} = 12$ phase-cycling scheme using radiofrequency phase increments ϕ evenly distributed in the range 0 to 2π rad: $\phi(j) = \pi/N_{pc} \cdot (2j-1)$, where j = 1, 2, ... N_{pc}. The bSSFP imaging protocol employed an isotropic resolution of $1.3 \times 1.3 \times 1.3$ mm^3 with an image encoding matrix of $176 \times 176 \times 128$, ensuring coverage of the entire brain. The repetition time TR and echo time TE were set to 4.8 ms and 2.4 ms, respectively, and the nominal flip angle α_{nom} was fixed at 15°. Prior to the acquisition of each phase-cycle ϕ, 256 dummy pulses were played out to establish steady-state conditions. Incorporating a 2-fold in-plane parallel imaging (Generalized Autocalibrating Partial Parallel Acquisition (GRAPPA)) acceleration factor, the acquisition of whole-brain 12-point pc-bSSFP data was completed within 10 min and 12 s. The B_1^+ scaling factor ($\alpha_{act}/\alpha_{nom}$ = actual/nominal flip angle) was calculated employing the vendor's standard B_1^+ mapping sequence[28,29], including a TR/TE/α_{nom} of 14.2 s/2.4 ms/8°, 30 sagittal slices with a 100% slice gap, an in-plane resolution of 2.4×2.4 mm^2, a slice thickness of 3 mm, and a total scan time of 29 s.

Data Processing *In Vivo*

Registration and segmentation tasks were performed using the FSL[30] and SPM[31] software packages. To correct for motion over the course of the 10 min scan, intra-registration along the phase-cycle dimension was achieved by registering the magnitude of each phase-cycle to the magnitude of the sixth phase-cycle and applying each transformation to the corresponding phase data. In addition, rigid body registration was used to align the B_1^+ baseline anatomical image to the mean magnitude image from the motion-corrected pc-bSSFP data. The obtained transformation was applied to the B_1^+ map, which was then 3D median
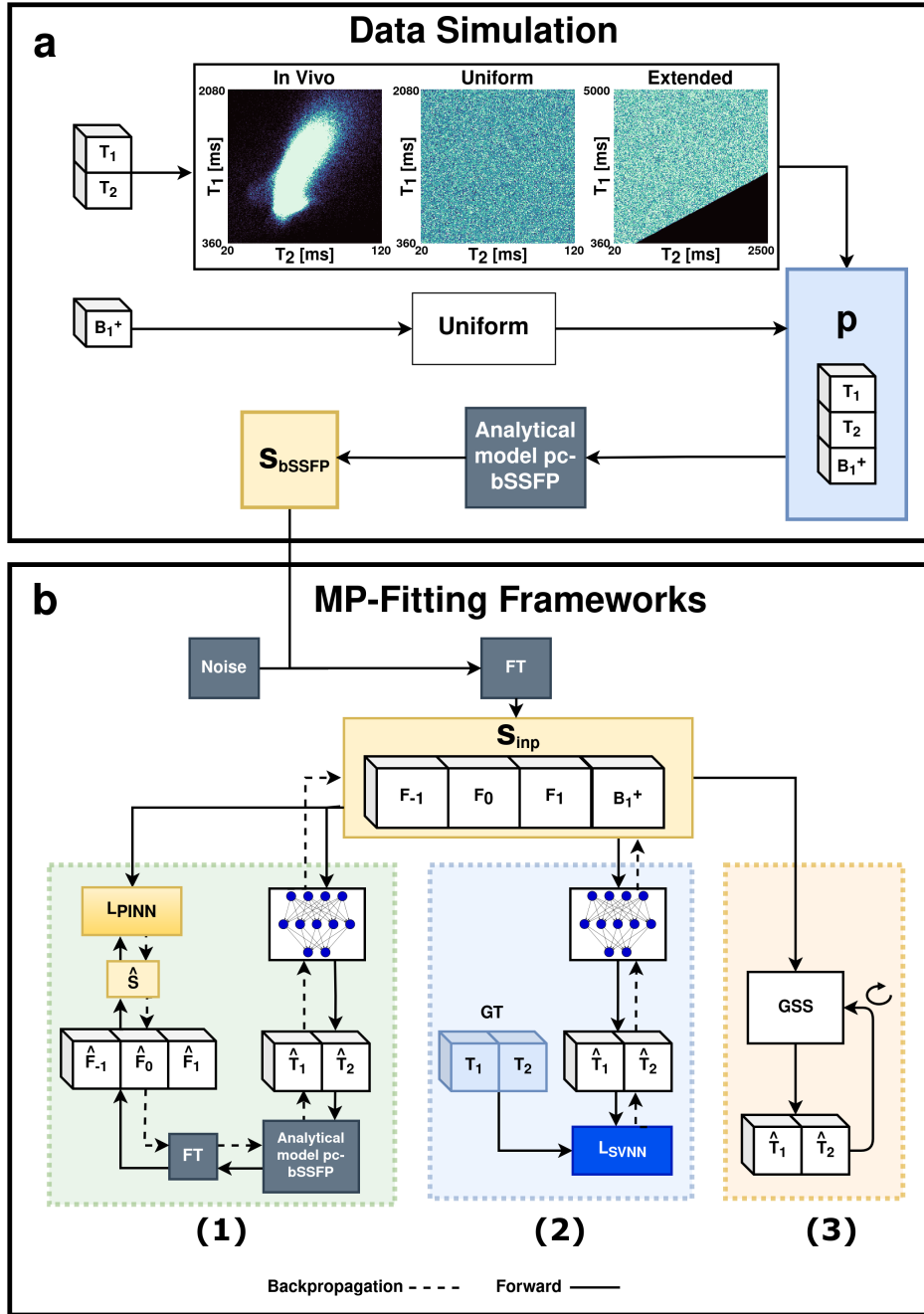
Figure 1. The workflow proposed in this work. (**a**) **Data Simulation:** The input parameters $\mathbf{p} = \left\{ T_1, T_2, B_1^+ \right\}$ entering the analytical bSSFP signal model (see Equation 1) were sampled from three different distributions (in vivo, uniform, and uniform extended) for T_1 and T_2, and from a single uniform distribution for B_1^+. The sequence parameters from the in vivo acquisition protocol (TR, TE, α_{nom}, N_{pc}) were used to draw 400,000 signal samples S_{bSSFP} from each T_1 and T_2 distribution. (**b**) **Multi-Parametric-Fitting Frameworks:** The input to each of the three frameworks, which means the physics-informed neural network (PINN, 1), the supervised neural network (SVNN, 2), and the iterative golden section search (GSS) fitting (MIRACLE, 3), consisted of the amplitudes of the three lowest order SSFP configuration modes computed from a Fourier transform (FT) of the phase-cycled bSSFP signal with the option to add noise and in addition of B_1^+. 1) and 2) use the same multilayer perceptron architecture to estimate the inverse signal model and predict the parameters $\hat{T}_1$ and $\hat{T}_2$. 1) uses the predicted $\hat{T}_1$ and $\hat{T}_2$ to generate an estimated signal $\hat{S}$ and compare it to the input signal S_{inp} in the L_{PINN} loss, while 2) compares the predicted $\hat{T}_1$ and $\hat{T}_2$ directly to the respective ground truth (GT) T_1 and T_2 in the L_{SVNN} loss.

filtered (kernel size $= [10, 10, 10]$). The three lowest order SSFP configuration modes F_{-1}, F_0, and F_1 were computed based on a 12-point discrete Fourier transform of the complex pc-bSSFP data and the magnitudes of the configuration modes were further subjected to Gibbs ringing removal[32]. Voxel-wise normalization using Euclidean distance was performed to match the in silico data. For in vivo SNR determination, the average signal level was obtained as the mean signal in a whole-brain tissue mask applied to the magnitude of the F_0 configuration, pooled across three representative subjects. The average noise level was determined as the mean standard deviation in a background mask applied to the same data. The average SNR level pooled across all three subjects was 25. The definition of the masks for the in vivo SNR determination is illustrated in Supplementary Fig. S1.

Data Generation *In Silico*

Synthetic single isochromat pc-bSSFP signals S_{bSSFP} were generated using the forward on-resonant bSSFP signal model $S_{\mathbf{bSSFP}}(\mathbf{p}, \mathbf{u})$ with parameters $\mathbf{p} \in \left\{ T_1, T_2, B_1^+ \right\}$ (longitudinal relaxation time T_1; transverse relaxation time T_2; transmit field scaling factor $B_1^+ = \alpha_{act} / \alpha_{nom}$), sequence parameters $\mathbf{u} \in \left\{ \mathbf{TR}, \mathbf{TE}, \alpha_{nom}, N_{pc} \right\}$ (repetition time TR, echo time TE, nominal flip angle α_{nom}, number of phase cycles N_{pc}), and initial magnetization $M_0 = 1$[33]:

$$S_{bSSFP} = M_0 \frac{(1 - E_1)(1 - E_2 e^{-i\phi}) \sin \alpha_{act}}{C \cos \phi + D} e^{-TE/T_2} \tag{1}$$

with

$$E_{1,2} = e^{-TR/T_{1,2}} \tag{2}$$

$$C = E_2(E_1 - 1)(1 + \cos \alpha_{act}) \tag{3}$$

$$D = (1 - E_1 \cos \alpha_{act}) - (E_1 - \cos \alpha_{act})E_2^2 \tag{4}$$

and

$$\phi[0, 2\pi] = \pi/N_{pc} \cdot (2j - 1), j = 1, 2, ..., N_{pc} \tag{5}$$

The target parameters T_1 and T_2 were sampled from three different distributions (see Figure 1): a uniform distribution with T_1 ranging from 360 to 2080 ms and T_2 ranging from 20 to 120 ms, a uniform distribution with an extended T_1 range from 360 to 5000 ms and an extended T_2 range from 20 to 2500 ms, and an in vivo distribution with the same range as the uniform distribution, but by sampling from a 2D density map generated based on the T_1 and T_2 brain voxel distributions of three healthy subjects obtained from existing gold standard 2D multi-slice inversion-recovery turbo-spin-echo (T_1) and 2D multi-slice single-echo spin-echo (T_2) scans with variable inversion and echo times, respectively. Corresponding anatomical magnetization-prepared rapid gradient-echo (MPRAGE) data[34] were skull-stripped and used for white matter (WM), gray matter (GM), and cerebrospinal fluid (CSF) segmentation. Voxels containing pure CSF according to the performed segmentation were excluded from the density estimation. The T_1 and T_2 parameter boundaries of the in vivo and uniform distribution were approximated as the mean $\pm$ 2 standard deviations of the values in the defined brain masks of three subjects. Additionally, $T_1 < T_2$ parameter combinations were excluded for all distributions. For each distribution, 400,000 samples were generated, resulting in a total training data size of 38.4 MB and 6.4 MB for the input and target data, respectively. B_1^+ was uniformly sampled in the range 0.7 to 1.3 and an on-resonant condition with an off-resonance $\Delta B_0 = 0$ Hz was assumed. Sequence parameters were set according to the in vivo pc-bSSFP protocol. For in silico performance validation, an additional 2D grid (200 x 200 steps) of linearly sampled T_1 and T_2 values in the uniform distribution range as well as 40,000 in vivo test data points sampled from the 2D in vivo density map were generated for pc-bSSFP signal simulation ($B_1^+ = 1$).

Relaxometry

For direct comparison, the DNNs were designed to take the same input data as MIRACLE, i.e. the magnitude of the three lowest order SSFP configuration modes (F_{-1}, F_0, F_1) and B_1^+, as shown in Figure 1. MIRACLE fitting was performed using an iterative golden section search minimization algorithm with an initial T_1 estimate of 1000 ms[14,15]. SVNNs and PINNs were based on a fully connected feed-forward multilayer perceptron with four inputs, two hidden layers of 64 neurons each, followed by a ReLU activation function, and an output sigmoid layer of two neurons for T_1 and T_2 estimation. The resulting

model contained 4610 trainable parameters, leading to a total size of 21 kB. The trainable parameters were initialized using PyTorch's default layer initialization[35] and the Adam optimizer[36]. A fixed learning rate of $2 \cdot 10^{-4}$, a batch size of 128, an early stopping with a patience of 25 epochs, and a maximum of 300 epochs were used for DNN training. Within each training batch, the real and imaginary parts of the pc-bSSFP data were corrupted by additive Gaussian noise samples with a noise level of $\eta = 0.074/(\sqrt{2} \cdot \text{SNR})$ and $\text{SNR} \in \{\inf, 50, 25, 10\}$, where η is zero if $\text{SNR} = \inf$. The three lowest order SSFP configuration modes were computed as described above in the subsection *Data Processing In Vivo*. While both DNN frameworks were designed to decode the inverse signal model from the pc-bSSFP signals to target relaxometry parameters, two different loss strategies were used as proposed by Grussu et al.[27]: a signal loss $L_{\text{PINN}} = \text{MSE}(\hat{S}, S_{inp})$ involving the analytical pc-bSSFP signal model and subsequent Fourier transform of the complex signal in the encoding step to compute the mean squared error (MSE) between the signal from the predicted target parameters $\hat{S}$ and the input signal S_{inp} (see Figure 1b, part 1), and a target parameter loss $L_{\text{SVNN}} = \text{MSE}(T_i, \hat{T}_i)$ with $i = 1, 2$, which computes the MSE between the model parameter predictions $\hat{T}_1$ and $\hat{T}_2$ and the ground truth target parameters T_1 and T_2 (see Figure 1b, part 2).

Validation *In Silico*

Each DNN framework, trained with different distributions and SNR levels, as well as the MIRACLE framework were validated on 5000 MC samples by augmenting the complex pc-bSSFP signals from the 2D linear grid and in vivo distribution test data of T_1 and T_2 values with additive noise from a Gaussian distribution and $\text{SNR} \in \{\inf, 50, 45, 40, 35, 30, 25, 20, 15, 10\}$. To test the accuracy and precision of each framework on in silico data, the mean μ_{MC}, standard deviation σ_{MC}, and relative standard deviation $\sigma_{rel} = \sigma_{\text{MC}}/\mu_{\text{MC}}$ of the parameter predictions across all MC samples were calculated. The relative error between the MC mean of the parameter predictions $\hat{y}_{\mu_{\text{MC}}}$ and the respective ground truth value y was calculated for both DNN frameworks on the 2D linear T_1 and T_2 sampling grid as $\varepsilon_{rel} = (\hat{y}_{\mu_{\text{MC}}} - y)/y \cdot 100$. In addition, the coefficient of determination (CoD) was calculated for all frameworks, distributions, and SNR levels for the entire 2D grid and the in vivo test data. The CoD was computed as a global metric as follows:

$$\text{CoD} = 1 - \frac{\sum_{i=1}^{n} (y_i - \hat{y}_{i_{\mu_{\text{MC}}}})^2}{\sum_{i=1}^{n} (y_i - \bar{y})^2} \tag{6}$$

where:

n is the number of observations,

y_i is the observed value for the ith observation,

$\hat{y}_{i_{\mu_{\text{MC}}}}$ is the MC mean of the predicted values for the ith observation,

$\bar{y}$ is the mean of the observed values.

Validation *In Vivo*

For each relaxometry framework, simultaneous whole-brain T_1 and T_2 estimation was performed in healthy subjects. SVNN and PINN frameworks trained without the addition of noise during training ($\text{SNR} = \inf$) were used for in vivo inference. To compare the effect of different training data distributions on prediction accuracy, the absolute difference between the DNN predictions from the trainings with three distributions and the MIRACLE prediction was calculated. In addition, MC sampling was performed on an exemplary axial slice of the in vivo data with 5000 samples and six augmented ROIs with additional Gaussian noise added to the real and imaginary parts of the acquired pc-bSSFP data before calculating the SSFP configuration modes.

The effectiveness of the DNN frameworks to learn the inverse signal model for MP-qMRI was investigated by calculating the CoD between whole-brain relaxometry predictions of each epoch and the final epoch of a training process for whole-brain WM, GM, and WM+GM tissue masks. Furthermore, a single-epoch PINN training was performed and applied to the in vivo test subject. The entire process of in silico data generation, single-epoch learning, and in vivo inference was timed and compared to the MIRACLE algorithm on whole brain pc-bSSFP data (single CPU thread on Intel(R) Xeon(R) W-2255 CPU @ 3.70GHz, 62.5 GB RAM). To assess the benefit of the trained DNN frameworks, the inference time for simultaneous in vivo whole-brain relaxometry was additionally measured for all three frameworks on input data interpolated to different isotropic resolutions of 1.3 mm, 1.0 mm, 0.8 mm, 0.6 mm, and 0.4 mm.

Results

In Silico

The impact of including image noise explicitly into the DNN training process by adding noise of a predefined level to the in silico training data is analyzed by an MC sampling of the in silico test data for DNNs trained on three different training data

distributions (cf. Figure 2). To ensure comparability with the acquired in vivo data, the noise added during training was matched to the SNR of 25 present in the masked brain tissue of the in vivo pc-bSSFP data and applied to the test data. As evident from Figure 2, training DNN frameworks under non-ideal conditions with noise-corrupted training samples does not imply better accuracy on test data with equal SNR level. While the accuracy of PINNs trained on noise-corrupted data (Figure 2b, right) appears similar to that of PINNs trained on noise-free data (Figure 2a, right), SVNNs perform worse when training includes noise (Figure 2, left). Furthermore, it can be observed that the performance of the trained PINN models is largely independent of the training data distribution, in contrast to the SVNN frameworks. In the case of the uniform distribution with extended parameter range, the SVNN shows reduced accuracy compared to the other two distributions. Since training with additional noise evidently does not improve prediction performance, the following analysis focuses on the application of DNNs trained on noise-free in silico data. Therefore, the indication of SNR or noise levels refers in the following exclusively to the test data rather than the training data.

The prediction performance dependence of the DNNs trained with noise-free data and MIRACLE on the SNR of the in silico test data is evaluated in Figure 3 by the calculation of the CoD, reflecting the agreement between the mean MC predictions and the ground truth for test data from a linear sampling grid (cf. Figure 3, left column) and from the in vivo distribution (cf. Figure 3, right column). High CoD values can be observed for MIRACLE at SNR levels down to $\approx 15 - 20$ until the accuracy starts to break down (cf. Figure 3a). While the difference between the CoD of the DNNs and MIRACLE (ΔCoD) is neglectable for high test SNR levels, the performance of the DNNs trained with the uniform and in vivo distributions is superior to MIRACLE at low SNR levels (≤ 15) (cf. Figure 3b and c). The DNNs trained with the uniform extended distribution show reduced CoD values on noisy test data comparable to MIRACLE. Only exception is the SVNN-based T_2 estimation, which shows a clearly lower accuracy than MIRACLE for the in vivo distribution test data in case of the uniform extended training data distribution (cf. Figure 3c, right).

The robustness of the DNNs trained with data distributions matched to the in vivo tissue T_1 and T_2 range, i.e. uniform and in vivo distributions, is further corroborated by the precision analysis in Figure 4. The relative standard deviation $\sigma_{rel}(T_i)$ of the MC simulation for in silico test data from a linear grid with an SNR $= 25$ reflecting in vivo conditions is lower than MIRACLE for both SVNNs and PINNs trained with the uniform or in vivo distribution while the DNNs trained with the uniform extended distribution demonstrate similar precision as MIRACLE. The performance advantage of the DNNs trained with the uniform and in vivo distribution is enhanced in low SNR scenarios (see Supplementary Fig. S2, SNR = 10).

In Vivo

In line with the in silico results in Figure 2 and Figure 3, the trained DNNs show high agreement with MIRACLE relaxometry in brain tissues when tested on unseen in vivo data, especially for the parameter distributions, which are optimized for brain tissue at the employed field strength (cf. Figure 5). The relaxation parameter values predicted by the SVNN framework, which was trained with the uniform extended distribution and thus for a parameter range covering not only relaxation times in tissues but also in fluids, deviate from T_1 and T_2 provided by MIRACLE. On the other hand, the PINN framework shows greater robustness to the underlying training data distribution with lower differences to the MIRACLE predictions, especially for T_2, but also T_1. Furthermore, the in vivo MC sampling demonstrates an increased precision (lower σ_{MC}) for DNNs trained with the uniform (cf. Figure 6) and in vivo (not shown) distributions as compared to MIRACLE, thus confirming the in silico findings illustrated in Figure 4. In accordance with the in silico results, mean and standard deviation of in vivo MC samples match the MIRACLE performance for DNNs trained with the uniform extended distribution (see Supplementary Fig. S3).

Flexible and Cost-Effective Relaxometry

The adaptability and flexibility of in silico DNN training is evaluated in Figure 7a (SVNN) and Figure 7b (PINN) by the CoD between the in vivo predictions of each epoch and the final epoch in different whole-brain tissue masks as well as the overall validation loss across epochs, representatively for a DNN training using the uniform data distribution. Final training convergence with a CoD > 0.99 was reached after about 200 epochs. However, already within the first epochs, T_1 and T_2 relaxation times of brain tissues are learned effectively. This is corroborated by CoD values higher than 0.93 and 0.88 after the very first, and higher than 0.99 and 0.97 after the first ten epochs for the SVNN (cf. Figure 7a) and PINN (cf. Figure 7b), respectively, across all investigated tissue masks. Training of a single epoch was completed after only about 9 s for the SVNN and 14 s for the PINN frameworks using a single CPU thread. The effectiveness of single-epoch versus final-epoch training is demonstrated for in vivo whole-brain relaxometry in Figure 7c and d for the SVNN and PINN frameworks, respectively. The entire process of training data simulation, single-epoch model training, and whole-brain in vivo inference at 1.3 mm isotropic resolution took only about 12 s and 17 s for the SVNN and PINN frameworks, respectively, thus only about 45 % and 64 % compared to the inference time of the MIRACLE algorithm applied to the same data by using the same computing power.

A clear advantage of using DNNs over the MIRACLE framework for simultaneous whole-brain relaxometry is the inference time, as demonstrated in Figure 8. When the resolution of the in vivo input data is increased from 1.3 mm to 0.8 mm or even to 0.4 mm isotropic voxel sizes, the inference time increases exponentially from 26.7 s to 96.9 s to 769.8 s for MIRACLE,
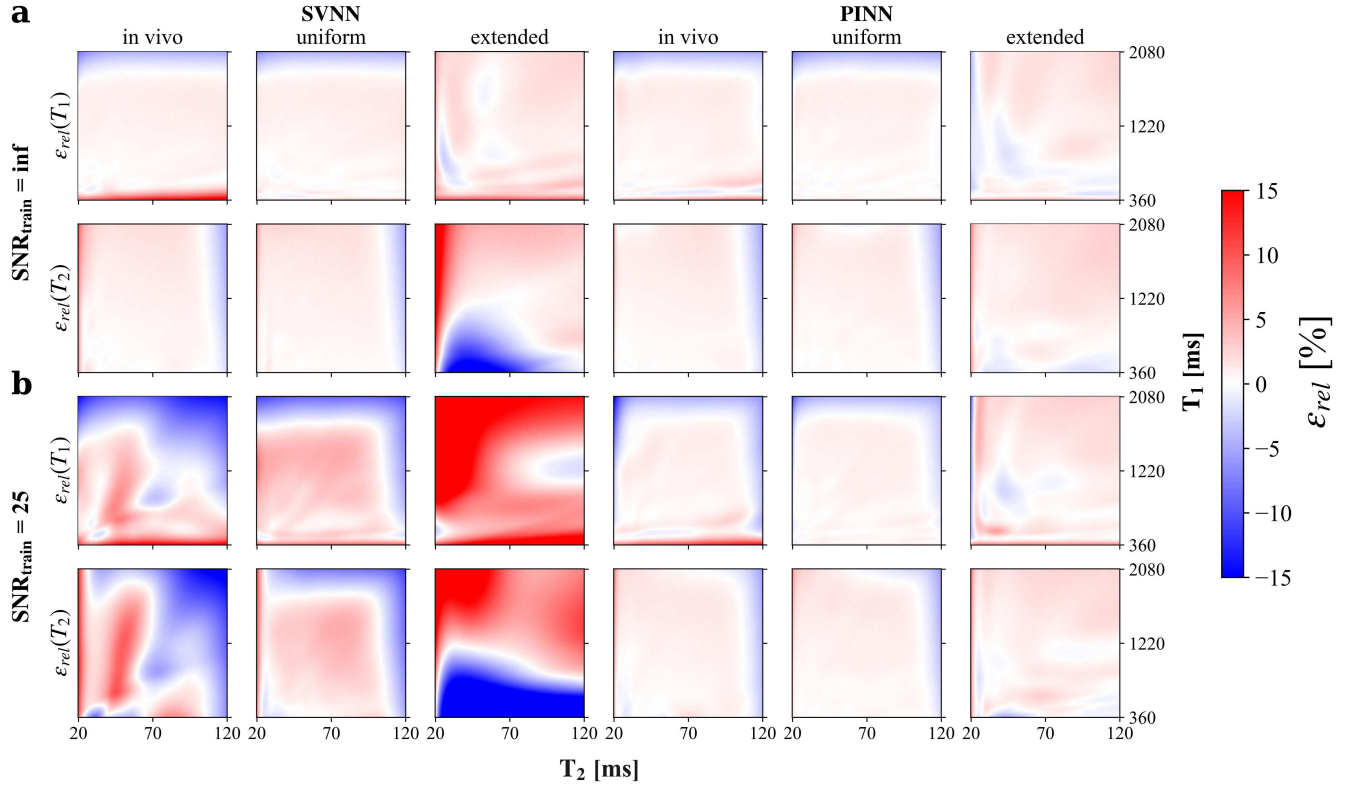
Figure 2. Influence of training data SNR and training data distribution on accuracy of investigated DNNs in silico. The relative error in percent $\varepsilon_{rel}(T_i) = (\hat{T}_{i_{\mu_{MC}}} - T_i)/T_i \cdot 100$ with $i = 1, 2$, between the mean of the MC simulation $\hat{T}_{i_{\mu_{MC}}}$ and the ground truth T_i, is quantified for T_1 and T_2 parameter estimates of the SVNNs (left) and PINNs (right) trained on noise-free (**a**, SNR = inf) and noise-corrupted (**b**, SNR = 25) data with different training data distributions. The MC estimation is performed on a noise-corrupted in silico linear test grid with SNR = 25 matched to in vivo conditions as well as a T_1 and T_2 range corresponding to brain tissues (consistent with the parameter range of the in vivo and uniform distribution employed for DNN training). Parameter over- and underestimation with respect to the ground truth are shown in red and blue, respectively.
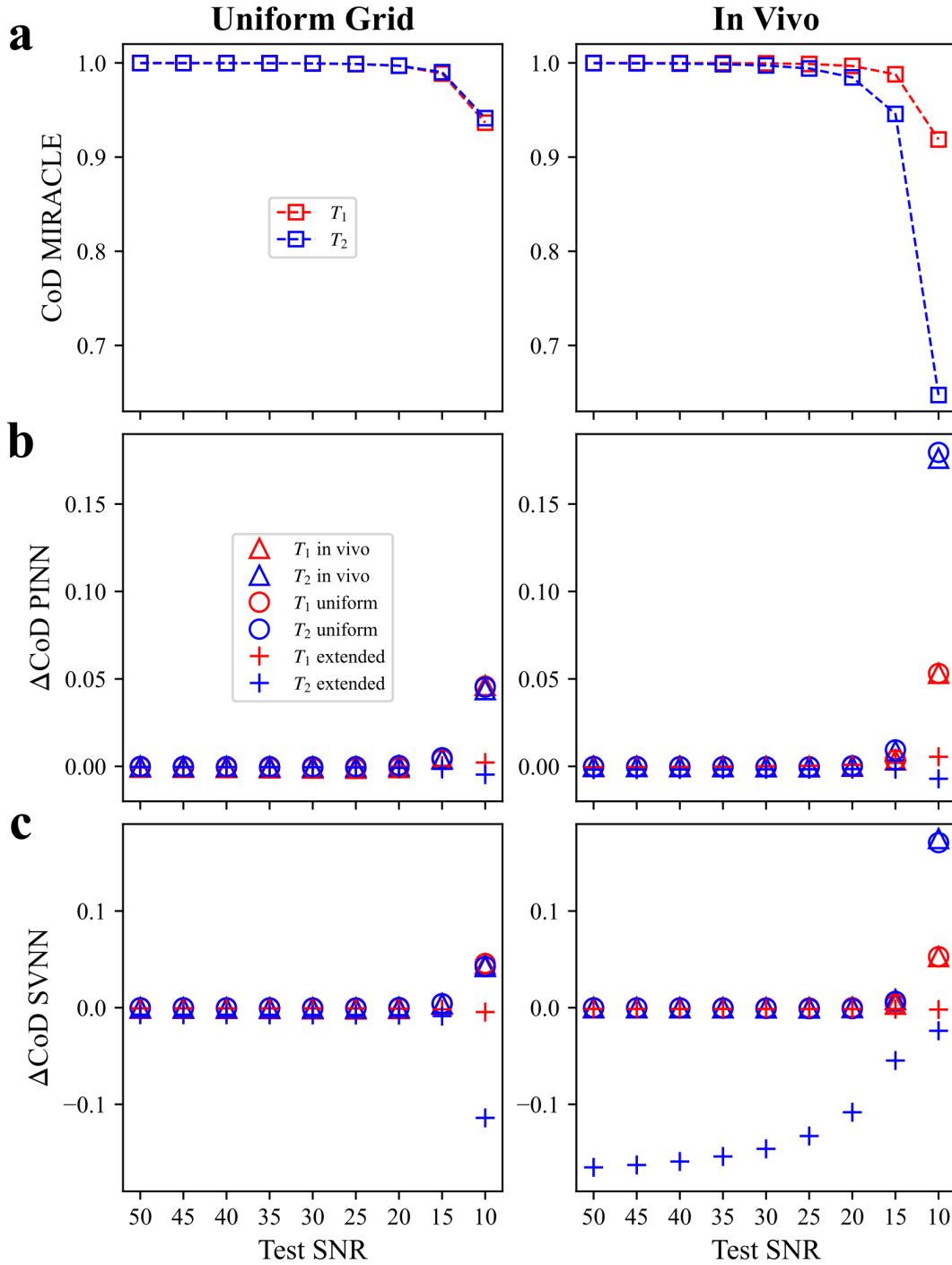
Figure 3. Coefficient of determination versus test data SNR of investigated DNNs relative to MIRACLE in silico. The CoD between the mean MC relaxation parameter predictions $\hat{T}_{i_{\mu_{MC}}}$ and the ground truth T_i with $i = 1, 2$ (T_1 in red and T_2 in blue) is shown for the linear test grid (left column) and the in vivo distribution test data (right column). (**a**) CoD versus test data SNR for MIRACLE ($\square$). (**b**) and (**c**) The absolute CoD difference between the DNNs and MIRACLE ($\Delta\text{CoD} = \text{CoD}_{\text{DNN}} - \text{CoD}_{\text{MIRACLE}}$) versus test data SNR for the PINN (**b**) and the SVNN (**c**). For both SVNN and PINN, three models trained on noise-free data (SNR = inf) with different data distributions are evaluated: in vivo ($\triangle$), uniform ($\circ$), and uniform extended distribution ($+$). Note that positive/negative values in (**b**) and (**c**) are referring to higher/lower CoD values of the DNNs relative to MIRACLE.
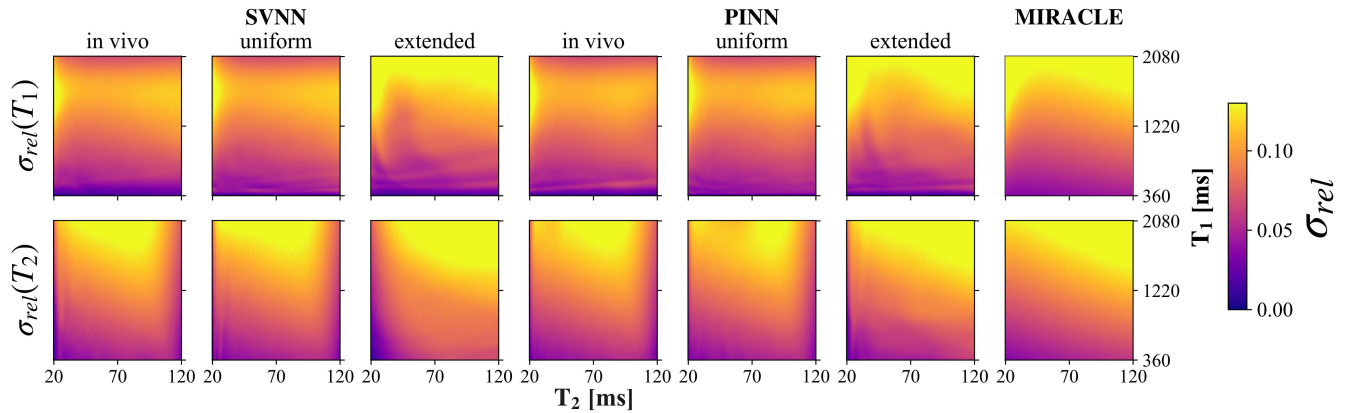
Figure 4. Influence of training data distribution on precision of investigated DNNs versus MIRACLE in silico. The precision of T_1 and T_2 quantification is evaluated by MC sampling with an **SNR level of 25**, matched to the in vivo data, applied to an in silico linear test grid with T_1 in the range 360 to 2080 ms and T_2 in the range 20 to 120 ms. The relative standard deviation $\sigma_{rel} = \sigma_{MC}/\mu_{MC}$, with μ_{MC} and σ_{MC} corresponding to the mean and standard deviation of the MC simulation is plotted for all three frameworks (SVNN, PINN, MIRACLE) and in case of the DNNs for all three trained data distributions. All DNNs were trained without additional noise applied to the training data (SNR = inf).

compared to 2.3 s to 9.9 s to 78.0 s for the PINN (and similarly for the SVNN). The inference time using DNNs is thus always in the order of one magnitude lower, allowing fast parameter estimation for very high-resolution whole-brain data in only about 10 % of the inference time compared to MIRACLE.

Discussion

Since the optimization of DNN model architectures may require new measurements, re-running of DNN training, or adaptation to changing tissue parameter characteristics at different field strengths as in case of relaxation times, flexible and effective DNN frameworks are desired. The results presented in this work suggest the combination of in silico trained DNNs with pc-bSSFP imaging as a fast and adaptable framework for MP-qMRI relaxometry. In silico DNN training allows full control over sequence parameters and tissue parameter distributions, does not require any extra measurements of ground truth data, and is able to efficiently learn the inverse signal model. Both supervised and self-supervised physics-informed DNNs have been successfully implemented and trained on different in silico data distributions, achieving a performance matching or exceeding the one of reference iterative multi-parametric fitting approaches such as MIRACLE with whole-brain in vivo inference times on unseen test data, which are an order of magnitude shorter in comparison to MIRACLE.

　　MC simulations based on in silico data (cf. Figure 2) revealed a strong sensitivity of SVNN estimation accuracy to the training data distribution, but also to the SNR level of the training data while the PINN models remained highly unaffected by the distribution and noise characteristics of the training samples. Generally, the DNNs trained on noise-corrupted training data and tested on data at the same SNR level did not reveal any ability to improve T_1 and T_2 prediction performance as compared to DNNs trained without any additional noise. Increasing the complexity of DNNs may allow to capture the noise present in the training data. However, sample-wise noise addition may be unrealistic for the spatially varying noise characteristics encountered in reconstructed MR images and hinder efficient learning of the signal model, especially for smaller DNN architectures with fewer trainable parameters. Provided the accessibility of larger cohort data sets, image-based DNNs could be investigated in future for denoising tasks.

　　The DNNs trained on noise-free in silico data with a uniform parameter distribution matched to the relaxation time range of tissues or an in vivo parameter distribution performed reliably in the presence of noise on the test data, with an advantage over MIRACLE for low SNR scenarios (cf. Figure 3), which may be particularly beneficial for potential future applications at low-fields ($B_0 \leq 1.5$ T). As evident from the results presented in Figure 4 for a realistic pc-bSSFP SNR level applied to the test data (determined for 3T and 1.3 mm isotropic resolution), the precision of the trained DNNs is affected by the training data distribution. For distributions tailored to the relaxation time range of interest, DNNs show ability to reach higher precision than MIRACLE, motivating the optimization of DNN frameworks for targeted tissue parameter ranges. The lower the SNR of the input data, the more pronounced becomes the precision advantage of the DNNs over MIRACLE (cf. Supplementary Fig. S2).

　　The in silico results were successfully reproduced on in vivo test data, revealing a stronger dependence on the training data distribution of the SVNN framework compared to the PINN framework (cf. Figure 5). The observed influence of training data
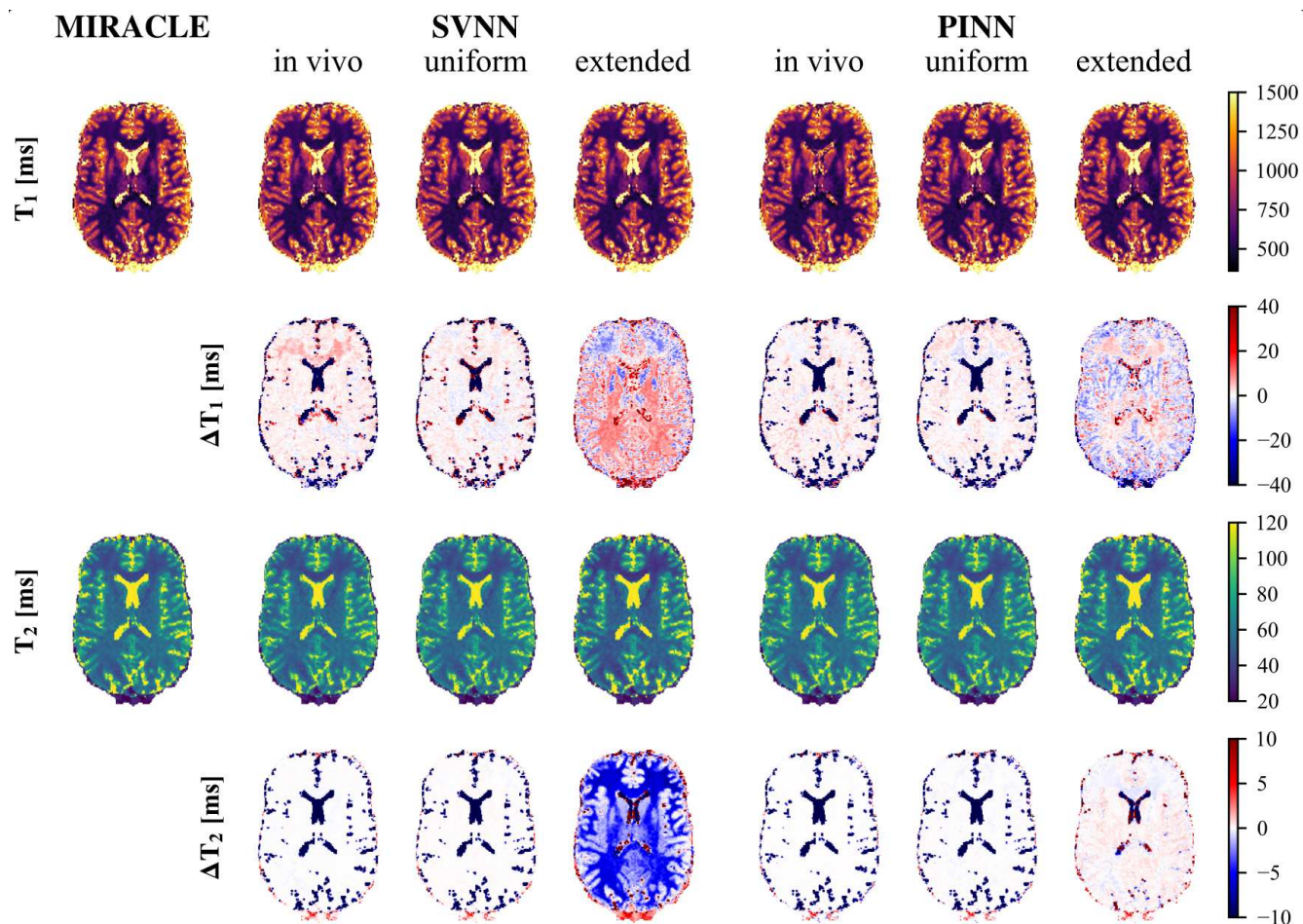
Figure 5. In vivo analysis of the effect of the DNN training data distribution relative to MIRACLE. A representative axial slice of the in vivo whole-brain T_1 (first row) and T_2 (third row) predictions of an unseen test subject is shown for the MIRACLE framework (first column), and both DNNs, each trained on in silico data without additional noise (SNR = inf) and three different distributions (in vivo, uniform, and uniform extended). The absolute differences between the DNN predictions and the MIRACLE prediction are shown in the second and fourth row for T_1 and T_2, respectively. Red and blue refer to an over- and underestimation of the DNN framework predictions relative to the MIRACLE framework predictions, respectively.
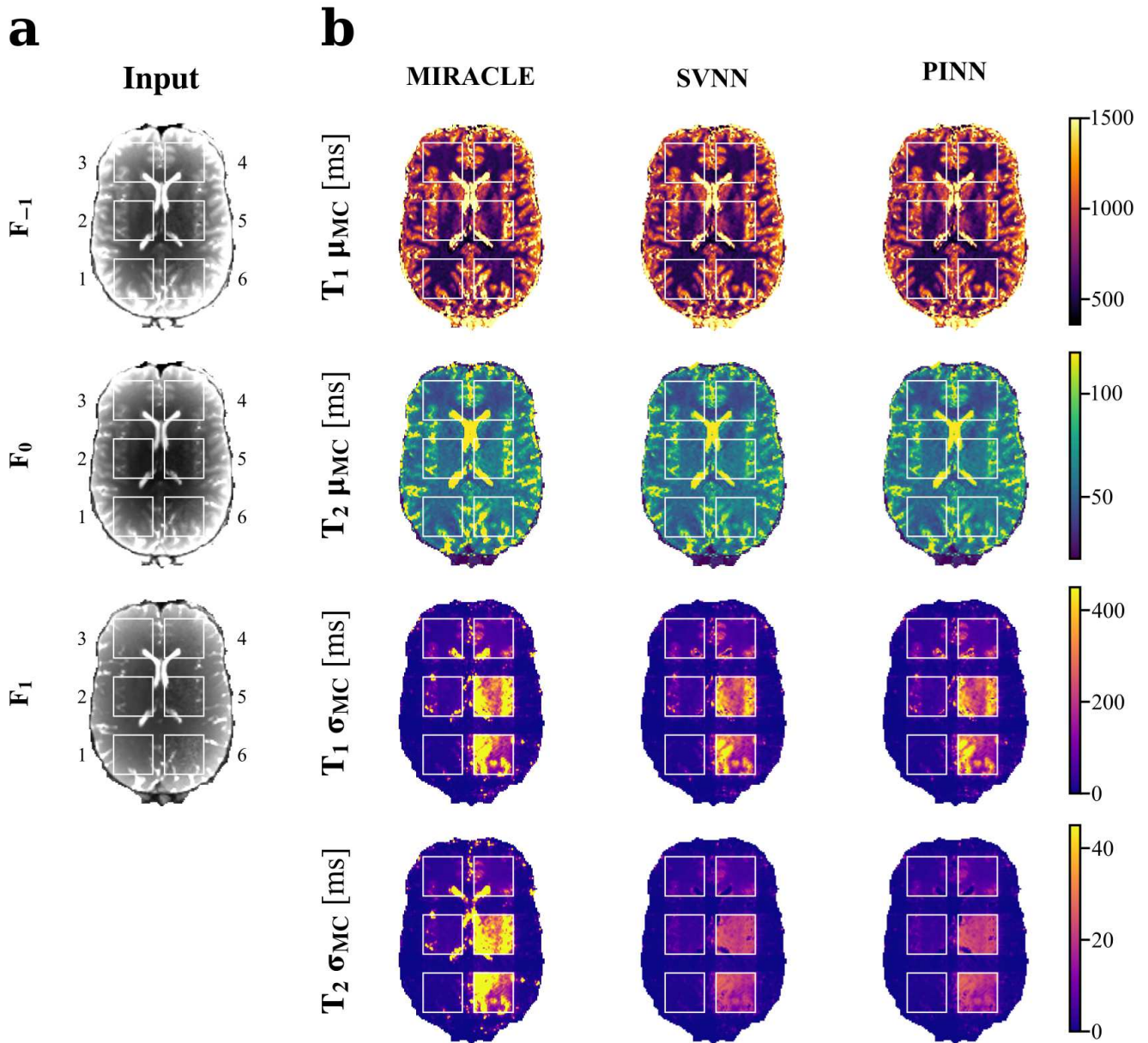
Figure 6. Robustness in the presence of noise-corrupted in vivo test data of SVNN and PINN versus MIRACLE, illustrated for a representative axial slice of an unseen test subject. (**a**) The multi-contrast input for quantification of the relaxation parameters, i.e. the magnitude of F_{-1}, F_0, and F_1, for an individual MC noise sample. (**b**) The mean (μ_{MC}, rows 1+2) and standard deviation (σ_{MC}, rows 3+4) of the in vivo MC parameter predictions. The displayed results refer to DNNs trained on in silico data with the **uniform distribution** and no additional noise (SNR = inf). In addition to the existing noise of the in vivo test data, noise sampled from a Gaussian distribution with six different standard deviations ($\eta \in \{1, 2, 4, 8, 12, 16\}$ and respective in vivo SNRs $\in \{18, 14, 11, 7, 5, 4\}$) was added to the real and imaginary parts of the pc-bSSFP data in six different rectangular ROIs, labeled 1-6 in the order of increasing noise levels.
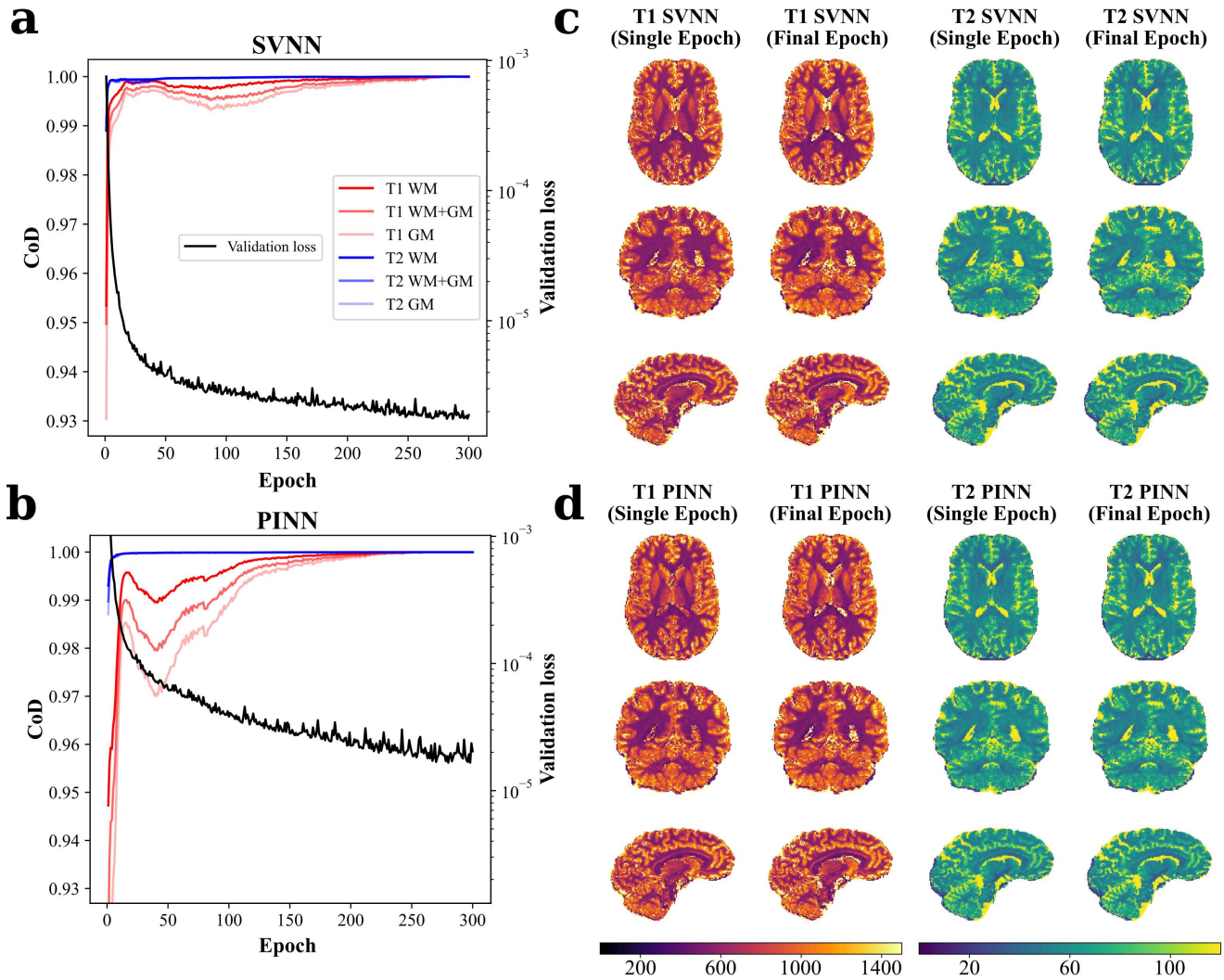
Figure 7. Efficiency of DNN inverse signal model learning versus epochs, corroborated by representative relaxation time maps of single-epoch in vivo whole-brain inference. The CoD during SVNN (**a**) and PINN (**b**) training is calculated for each epoch with respect to the final-epoch model and plotted versus epochs for in vivo T_1 (red) and T_2 (blue) predictions in whole-brain WM, GM, and WM+GM tissue masks of an unseen test subject. Additionally, the validation loss for both DNN frameworks is shown in black on a logarithmic scale. The employed DNNs were trained on the in silico uniform noise-free data distribution. Note that the final validation loss of the SVNN framework is on the order of one magnitude lower than the one of the PINN framework due to the different definitions of the loss functions and embedding of physical constraints for the PINN. Corresponding representative axial, coronal, and sagittal slices of in vivo whole-brain T_1 and T_2 single-echo versus final-epoch predictions of an unseen test subject are shown for SVNN (**c**) and PINN (**d**).
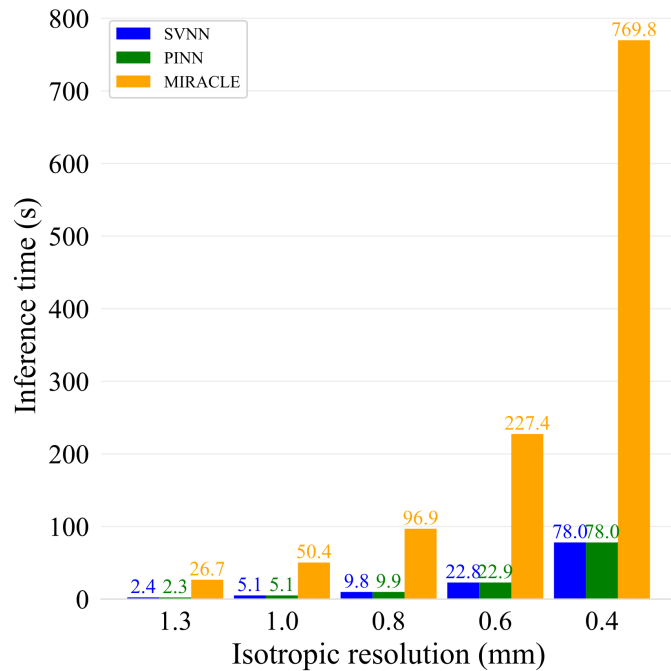
Figure 8. Whole-brain relaxometry inference times for different isotropic resolutions of the input data. The inference times in seconds of each multi-parametric relaxometry framework (SVNN: blue, PINN: green, MIRACLE: orange) are calculated for the whole-brain input data of a test subject interpolated to different isotropic resolutions of 1.3, 1.0, 0.8, 0.6 and 0.4 mm. Inference is performed using a single CPU thread (Intel(R) Xeon(R) W-2255 CPU @ 3.70GHz, 62.5 GB RAM).

distribution on the accuracy of SVNNs is consistent with existing research[26, 37]. Epstein et al. proposed to adjust the in silico ground truth labels by precomputed labels from maximum likelihood estimation and to extend the supervised loss to improve the accuracy of SVNNs[37]. On the other hand, the observed robustness of physics-informed DNNs to the underlying training data distributions can be explained by a successful utilization of the analytical pc-bSSFP signal model, which encodes the estimated parameters into the pc-bSSFP signal during the learning process. Additionally, we observed that the DNNs, which were trained on data distributions optimized for the brain tissue parameter range, achieved lower standard deviations in the in vivo MC simulations for added noise levels and thus increased precision compared to MIRACLE (cf. Figure 6), in line with the in silico findings.

Inherent to the architecture of PINNs are the boundaries of the achievable parameter values, which are predefined by the developer, prohibiting extrapolation. Thus, a limitation of PINNs is the need for retraining if the parameter range of interest falls outside the simulated range. Similarly, the performance of SVNNs is expected to be impaired for parameter combinations not contained in the training set. Furthermore, this work is restricted to a single-component signal model by assuming that only a single T_1 and T_2 component at a single resonance frequency contributes to the acquired pc-bSSFP signal evolutions in tissues, thus not accounting for characteristic asymmetries in the frequency response of bSSFP. Those reflect anisotropies in tissue microstructure with a correlation to diffusion metrics, e.g. in WM[38–41], or the sensitivity to chemical shift, which can be exploited for fat fraction mapping[42]. Comparable to MIRACLE, this results in an underestimation of T_1 and T_2 in brain tissues with respect to gold standard spin-echo-based reference methods[15, 16].

In contrast to PINN, SVNN architectures are capable to identify nonlinear feature decodings, which cannot be modeled analytically. This can be exploited for the training of model-free SVNNs on in vivo data with independent ground truth MR measurements for each target parameter. However, supervised learning on in vivo data may be prone to input and target misalignment and necessitate prohibitively long scan times due to the need for ground truth data acquisition. Furthermore, the common ground in qMRI is dynamic and even current gold standard methods can be subject to various adverse instrumental factors related to the underlying sequence, hardware, or fitting routine, potentially leading to a quantification bias[43].

Due to the ability to simulate, train, and infer tissue parameters in only a few seconds as demonstrated here (cf. Figure 7), in silico DNN training provides a cost-effective option and can easily be adapted to altered sequence parameters, new anatomical targets, or different field strengths, without requiring extensive MR data collection. While this work focuses on a direct comparison with MIRACLE, the input of the implemented DNNs can conveniently be extended to include phase information and thus to extract additional parameters, e.g. ΔB_0. Once trained, the investigated DNNs are able to infer multi-parametric

relaxation characteristics an order of magnitude faster than traditional iterative fitting as only a few matrix multiplications need to be performed (cf. Figure 8). This has high value in terms of clinical applicability or for studies necessitating the processing of large data cohorts. Future work may include the extension of the signal model employed for in silico DNN training to multi-compartment scenarios, the implementation of image-based architectures to benefit from anatomical information, and the application to pathological test data to validate the generalization performance in a clinical context.

In conclusion, we have derived adaptable cost-effective deep learning frameworks for multi-parametric relaxometry based on pc-bSSFP data, which are characterized by rapid convergence during training, parameter inference times of only a few seconds once training is concluded, and the ability to embed physical knowledge into the training process. By tailoring the underlying training data distribution to the target parameters of interest, superior performance to conventional fitting approaches could be achieved, especially in low-SNR scenarios, motivating further investigations at low field strengths.

Data availability

The data sets analysed during the current study are available via the data sharing platform KEEPER. Upon request, a password-protected fully anonymized data set of a test subject can be downloaded.

Code availability

The source code and trained models for this study will be publicly available upon acceptance on Github.

References

1. Van Beek, E. J. *et al.* Value of MRI in medicine: More than just another test? *J. Magn. Reson. Imaging* **49**, e14–e25, DOI: 10.1002/jmri.26211 (2019).

2. Gracien, R.-M. *et al.* How stable is quantitative MRI? – Assessment of intra- and inter-scanner-model reproducibility using identical acquisition sequences and data analysis programs. *NeuroImage* **207**, 116364, DOI: 10.1016/j.neuroimage.2019.116364 (2020).

3. Granziera, C. *et al.* Quantitative magnetic resonance imaging towards clinical application in multiple sclerosis. *Brain* **144**, 1296–1311, DOI: 10.1093/brain/awab029 (2021).

4. Straub, S. *et al.* Quantitative magnetic resonance imaging biomarkers for cortical pathology in multiple sclerosis at 7 T. *NMR Biomed.* **36**, e4847, DOI: 10.1002/nbm.4847 (2023).

5. Sarkar, P., Sherwani, P., Dev, R. & Tiwari, A. Role of T2 relaxometry in localization of mesial temporal sclerosis and the degree of hippocampal atrophy in patients with intractable temporal lobe epilepsy: A cross sectional study. *Hippocampus* **33**, 1189–1196, DOI: 10.1002/hipo.23572 (2023).

6. Seiler, A. *et al.* Extent of Microstructural Tissue Damage Correlates with Hemodynamic Failure in High-Grade Carotid Occlusive Disease: An MRI Study Using Quantitative T2 and DSC Perfusion. *Am. J. Neuroradiol.* **39**, 1273–1279, DOI: 10.3174/ajnr.A5666 (2018).

7. Knight, M. J., Wearn, A., Coulthard, E. & Kauppinen, R. A. T2 Relaxometry and Diffusion Tensor Indices of the Hippocampus and Entorhinal Cortex Improve Sensitivity and Specificity of MRI to Detect Amnestic Mild Cognitive Impairment and Alzheimer's Disease Dementia. *J. Magn. Reson. Imaging* **49**, 445–455, DOI: 10.1002/jmri.26195 (2019).

8. Wearn, A. R. *et al.* T2 heterogeneity: a novel marker of microstructural integrity associated with cognitive decline in people with mild cognitive impairment. *Alzheimer's Res. & Ther.* **12**, 105, DOI: 10.1186/s13195-020-00672-9 (2020).

9. Gracien, R.-M. *et al.* Evaluation of brain ageing: a quantitative longitudinal MRI study over 7 years. *Eur. Radiol.* **27**, 1568–1576, DOI: 10.1007/s00330-016-4485-1 (2017).

10. Nürnberger, L. *et al.* Longitudinal changes of cortical microstructure in Parkinson's disease assessed with T1 relaxometry. *NeuroImage: Clin.* **13**, 405–414, DOI: 10.1016/j.nicl.2016.12.025 (2017).

11. Seiler, A. *et al.* Multiparametric Quantitative MRI in Neurological Diseases. *Front. Neurol.* **12**, 640239, DOI: 10.3389/fneur.2021.640239 (2021).

12. Jara, H. *et al.* Primary Multiparametric Quantitative Brain MRI: State-of-the-Art Relaxometric and Proton Density Mapping Techniques. *Radiology* **305**, 5–18, DOI: 10.1148/radiol.211519 (2022).

13. Bieri, O. & Scheffler, K. Fundamentals of Balanced Steady State Free Precession MRI. *J. Magn. Reson. Imaging* **38**, 2–11, DOI: 10.1002/jmri.24163 (2013).

14. Heule, R., Ganter, C. & Bieri, O. Triple echo steady-state (TESS) relaxometry. *Magn. Reson. Medicine* **71**, 230–237, DOI: 10.1002/mrm.24659 (2014).

15. Nguyen, D. & Bieri, O. Motion-Insensitive Rapid Configuration Relaxometry. *Magn. Reson. Medicine* **78**, 518–526, DOI: 10.1002/mrm.26384 (2017).

16. Shcherbakova, Y., van den Berg, C. A., Moonen, C. T. & Bartels, L. W. PLANET: An Ellipse Fitting Approach for Simultaneous T1 and T2 Mapping Using Phase-Cycled Balanced Steady-State Free Precession. *Magn. Reson. Medicine* **79**, 711–722, DOI: 10.1002/mrm.26717 (2018).

17. Heule, R., Celicanin, Z., Kozerke, S. & Bieri, O. Simultaneous multislice triple-echo steady-state (SMS-TESS) T_1, T_2, PD, and off-resonance mapping in the human brain. *Magn. Reson. Medicine* **80**, 1088–1100, DOI: 10.1002/mrm.27126 (2018).

18. Heule, R., Bause, J., Pusterla, O. & Scheffler, K. Multi-parametric artificial neural network fitting of phase-cycled balanced steady-state free precession data. *Magn. Reson. Medicine* **84**, 2981–2993, DOI: 10.1002/mrm.28325 (2020).

19. Ma, D. *et al.* Magnetic resonance fingerprinting. *Nature* **495**, 187–192, DOI: 10.1038/nature11971 (2013).

20. Ma, D. *et al.* Development of high-resolution 3D MR fingerprinting for detection and characterization of epileptic lesions. *J. Magn. Reson. Imaging* **49**, 1333–1346, DOI: 10.1002/jmri.26319 (2019).

21. Fang, Z. *et al.* Submillimeter MR fingerprinting using deep learning–based tissue quantification. *Magn. Reson. Medicine* **84**, 579–591, DOI: 10.1002/mrm.28136 (2020).

22. Khajehim, M., Christen, T., Tam, F. & Graham, S. J. Streamlined magnetic resonance fingerprinting: Fast whole-brain coverage with deep-learning based parameter estimation. *NeuroImage* **238**, 118237, DOI: 10.1016/j.neuroimage.2021.118237 (2021).

23. Cohen, O., Zhu, B. & Rosen, M. S. MR fingerprinting Deep RecOnstruction NEtwork (DRONE). *Magn. Reson. Medicine* **80**, 885–894, DOI: 10.1002/mrm.27198 (2018).

24. Hamilton, J. I. & Seiberlich, N. Machine Learning for Rapid Magnetic Resonance Fingerprinting Tissue Property Quantification. *Proc. IEEE* **108**, 69–85, DOI: 10.1109/JPROC.2019.2936998 (2020).

25. Cheng, C., Preiswerk, F. & Madore, B. Multi-pathway multi-echo acquisition and neural contrast translation to generate a variety of quantitative and qualitative image contrasts. *Magn. Reson. Medicine* **83**, 2310–2321, DOI: 10.1002/mrm.28077 (2020).

26. Gyori, N. G., Palombo, M., Clark, C. A., Zhang, H. & Alexander, D. C. Training data distribution significantly impacts the estimation of tissue microstructure with machine learning. *Magn. Reson. Medicine* **87**, 932–947, DOI: 10.1002/mrm.29014 (2022).

27. Grussu, F. *et al.* Deep Learning Model Fitting for Diffusion-Relaxometry: A Comparative Study. In Gyori, N. *et al.* (eds.) *Computational Diffusion MRI*, 159–172, DOI: 10.1007/978-3-030-73018-5_13 (Springer International Publishing, Cham, 2021). Series Title: Mathematics and Visualization.

28. Fautz, H.-P., MW, V., Gross, P., AB, K. & Zhu, Y. B1 Mapping of Coil Arrays for Parallel Transmission. *Proc Intl Soc Magn Reson. Med* **16** (2008).

29. Chung, S., Kim, D., Breton, E. & Axel, L. Rapid B_1^+ mapping using a preconditioning RF pulse with TurboFLASH readout. *Magn. Reson. Medicine* **64**, 439–446, DOI: 10.1002/mrm.22423 (2010).

30. Jenkinson, M., Bannister, P., Brady, M. & Smith, S. Improved Optimization for the Robust and Accurate Linear Registration and Motion Correction of Brain Images. *NeuroImage* **17**, 825–841, DOI: 10.1006/nimg.2002.1132 (2002).

31. Friston, K. J., Ashburner, J., Kiebel, S. J., Nichols, T. E. & Penny, W. D. (eds.) *Statistical Parametric Mapping: The Analysis of Functional Brain Images* (Academic Press, 2007).

32. Veraart, J., Fieremans, E., Jelescu, I. O., Knoll, F. & Novikov, D. S. Gibbs ringing in diffusion MRI: Gibbs Ringing in Diffusion MRI. *Magn. Reson. Medicine* **76**, 301–314, DOI: 10.1002/mrm.25866 (2016).

33. Zur, Y., Wood, M. L. & Neuringer, L. J. Motion-insensitive, steady-state free precession imaging. *Magn. Reson. Medicine* **16**, 444–459, DOI: 10.1002/mrm.1910160311 (1990).

34. Mugler, J. P. & Brookeman, J. R. Three-dimensional magnetization-prepared rapid gradient-echo imaging (3D MP RAGE). *Magn. Reson. Medicine* **15**, 152–157, DOI: 10.1002/mrm.1910150117 (1990).

35. He, K., Zhang, X., Ren, S. & Sun, J. Delving Deep into Rectifiers: Surpassing Human-Level Performance on ImageNet Classification, DOI: 10.48550/ARXIV.1502.01852 (2015).

36. Kingma, D. P. & Ba, J. Adam: A Method for Stochastic Optimization, DOI: https://doi.org/10.48550/arXiv.1412.6980 (2017).

37. Epstein, S. C., Bray, T. J. P., Hall-Craggs, M. & Zhang, H. Choice of training label matters: how to best use deep learning for quantitative MRI parameter estimation, DOI: http://dx.doi.org/10.59275/j.melba.2024-geb5 (2022).

38. Miller, K. L. Asymmetries of the balanced SSFP profile. Part I: Theory and observation. *Magn. Reson. Medicine* **63**, 385–395, DOI: https://doi.org/10.1002/mrm.22212 (2010).

39. Miller, K. L., Smith, S. M. & Jezzard, P. Asymmetries of the balanced SSFP profile. Part II: White matter. *Magn. Reson. Medicine* **63**, 396–406, DOI: https://doi.org/10.1002/mrm.22249 (2010).

40. Heule, R. *et al.* Structure or Exchange? On the Feasibility of Chemical Exchange Detection with Balanced Steady-State Free Precession in Tissue – An In Vitro Study. *NMR Biomed.* **33**, DOI: https://doi.org/10.1002/nbm.4200 (2020).

41. Birk, F. *et al.* High-resolution neural network-driven mapping of multiple diffusion metrics leveraging asymmetries in the balanced steady-state free precession frequency profile. *NMR Biomed.* DOI: 10.1002/nbm.4669 (2021).

42. Rossi, G. M. C. *et al.* SPARCQ: A new approach for fat fraction mapping using asymmetries in the phase-cycled balanced SSFP signal profile. *Magn. Reson. Medicine* **90**, 2348–2361, DOI: 10.1002/mrm.29813 (2023).

43. Stikov, N. *et al.* On the accuracy of T$_1$ mapping: Searching for common ground. *Magn. Reson. Medicine* **73**, 514–522, DOI: 10.1002/mrm.25135 (2015).

Acknowledgements

Author contributions statement

Initial data collection: R.H. Conceptualization: F.B., R.H. Funding acquisition: K.S., R.H. Investigation: F.B., R.H. Method development: F.B., R.H. Method implementation: F.B., L.M., J.S., Q.W. Resources: K.S., R.H. DNN model training and testing: F.B. Supervision: R.H. Visualization: F.B. Writing—original draft: F.B., R.H. Writing—review & editing: F.B., L.M., J.S., Q.W., K.S., R.H.

Competing interests

The authors declare no competing interests.

Supplementary Files

This is a list of supplementary files associated with this preprint. Click to download.

- supplementary.pdf